



HAL
open science

Final Report of AMoSS : Advanced Modeling on Shear Shallow Flows for Curved Topography : water and granular flows

Boniface Nkonga

► **To cite this version:**

Boniface Nkonga. Final Report of AMoSS : Advanced Modeling on Shear Shallow Flows for Curved Topography : water and granular flows. [Research Report] INRIA Sophia Antipolis - Méditerranée. 2016. hal-01426859

HAL Id: hal-01426859

<https://inria.hal.science/hal-01426859>

Submitted on 20 Sep 2017

HAL is a multi-disciplinary open access archive for the deposit and dissemination of scientific research documents, whether they are published or not. The documents may come from teaching and research institutions in France or abroad, or from public or private research centers.

L'archive ouverte pluridisciplinaire **HAL**, est destinée au dépôt et à la diffusion de documents scientifiques de niveau recherche, publiés ou non, émanant des établissements d'enseignement et de recherche français ou étrangers, des laboratoires publics ou privés.



Inria international program

Final report

Associate Team acronym: AMoSS : Advanced Modeling on Shear Shallow Flows for Curved Topography : water and granular flows.

Period of activity:
2014 – 2016

Principal investigator (Inria):
Boniface Nkonga, CASTOR/Inria Sophia-Antipolis.

Principal investigator (partner):
Yih-Chin Tai, Associate Professor, National Cheng Kung University

Other participants:

- **Hervé Guillard**, senior researcher, CASTOR/INRIA Sophia-Antipolis,
- **Mario Ricchiuto**, researcher, CARDAMOM/INRIA Bordeaux,
- **Maria Kazolea**, researcher, CARDAMOM/INRIA Bordeaux,
- **Mathieu Colin**, associate professor, (CARDAMOM/INRIA) University of Bordeaux,
- **Sergey Gavriljuk**, Professor, University of Marseille
- **Olivier Delestre**, associate professor, University of Nice.
- **Chyan-Deng Jan**, Professor, National Cheng Kung University
- **Chih-Yu Kuo**, Associate Research Fellow, Center for App. Sciences, Academia Sinica
- **Keh-Ming Shyue**, Professor, National Taiwan University
- **Fuling Yang**, Associate Professor, National Taiwan University

Teams' web site: indicate the URL here.
<https://team.inria.fr/amoss/>

1. Scientific Achievements and perspectives

Our aim was to derive new models and numerical strategies for shear shallow flows on curved topography. This modeling was supported by physical and numerical experiments, investigations and validations. The initial scientific plan was organized in seven tasks. We will reconsider the initial tasks and gives some detail of the achievements of the last tree year's of collaboration.

Shear shallow water flows on locally cylindrical topography (2D to 1D).

Most of geophysical thin flows take place in complex topography: avalanches, landslides, debris flows, etc. There is a strong link between the flow path and the geometry of the basal topography. The terminology "shallow flow" is here used to characterize thin flows on curved surfaces. It is customary for this type of flows; to use the incompressible Naviers-Stokes equations to asymptotically derive reduced models for the evolution of the depth integrated speed and the thickness of the flow. Reduced model are mainly hyperbolic and finite volume method are often used

for their numerical approximation. Approximations strategies are generally structured as follow: 1) Construction of a global coordinate system associated with the assumption that the surface description is given analytically; 2) Reduction of the model relatively to the global coordinate system; 3) Approximation of the surface by a finite number of elements; 4) Approximation of the reduced model using the discrete surface.

In the context of real applications, it is presumptuous to expect an analytical formulation of the surface. From the data provided by geographic information system (GIS), we casually extract a discrete description of the surfaces that drives thin flow. Therefore, it is more practical to use the discrete description as the starting point of the resolution strategy. This is the angle of approach that we will consider in the following. Then we will locally define two mesh scales: the element scale and the cell scale. The discrete mapping and the reduced model are defined at the element scale and the average values that evolve in time are defined at the cell scale. We have derived a simple multidimensional Riemann solver that can be regarded as an actual two-dimensional generalization of the HLL Riemann solver and have provided closed form expressions for its implementation. The numerical tests have served to put in evidence the robustness and accuracy of the scheme.

Comparison with experimental results and unreduced model on flat plane.

The purpose of this work was the numerical study of the roll-waves that develop from a uniform unstable flow down an inclined rectangular channel. In particular, the formation of the roll-waves is studied by two different approaches. In the first approach, the roll-waves were produced in a long channel where a wave maker perturbed the free surface only at the channel inlet. The average discharge was fixed. In the second approach, the roll-waves were produced in a “periodic box” with a uniform flow velocity. The average depth of a perturbed free surface was the same as in the long channel. Formally, the “periodic box” and a long channel correspond to two different physical situations. However, the stationary profile formed for long time in these cases is the same. This allows us to use the “periodic box” as a simpler mathematical tool to study the asymptotic behavior of roll waves. In particular, the “periodic box” does not require a big space domain resolution. Several interesting phenomena were observed. First, it was proven that there exists L_{\max} such that any single roll wave of length $L > L_{\max}$ not stable. This can help to generalize the analytical results obtained by Liapidevskii (modulational stability study) and Baker et al. (the linear stability study) for the SV equations, to the case of the generalized models. The minimal length of periodic box for which a single roll wave is stable, was not observed. Second, a coarsening phenomenon was observed. When the inlet perturbation has two different frequencies, it produces the waves of the different wavelengths. The waves begin to interact. The short waves transfer their energy to the long waves, and finally we obtain the train of roll waves of a larger wavelength. A strong non-stationary modulation of the wave amplitude was observed. The formation of periodic roll wave train was shown for both long a channel and a “periodic box” for two sets of experimental parameters. In both cases, the free surface profile for the generalized models was found in a very good agreement with the experimental results. Finally, for a 2D simplified “Toy Model” we show that steady numerical solution corresponding to experimental data does not depend of transverse perturbations. Numerical methods for the “Toy Model” have been designed and comparisons with the experimental data on a channel experiment done by Yih-Chin Tai and his team in Tainan. The shear shallow flow models are also the subjects of collaboration with the Technical University of Crete (Prof Argyrus Delis) who visited Inria and the LJAD in June 2016.

Models for granular materials and laboratory measurements

Lateral boundary friction coefficient for continuum mathematical models

Research effort on modeling surface dry granular flows has been focused primarily on a feasible constitutive relation for bulk internal stress which is translated to a basal stress model when applied to depth-averaged models. When the flow is confined or strongly interacted with lateral obstacles, an effective model for lateral friction is also desired but much less investigated. The conventional expression takes the form of Coulomb friction, $\tau = \mu_w p$, in terms of a hydrostatic normal stress p and an effective wall friction coefficient μ_w which is often assigned to a material-dependent constant. Nonetheless, a series of laboratory experiments and compatible discrete element simulations for surface granular avalanche have been conducted and revealed non-constant μ_w .

Calibrate discrete element simulation framework for predictive simulation

Targeting surface hazardous flows, we chose the avalanche of finite granular mass down a narrow reservoir of smooth frictional bed as a benchmark problem (Figure 1/left). To have realistic simulation framework, we have developed a methodology to assign parameters in the linear soft-sphere contact model so that the DEM simulation can reproduce experimentally measured avalanche dynamics. With material elastic properties, the normal spring constant is assigned specifically to reproduce *Hertzian contact time* while the tangential spring constant is chosen according to elasticity theory. Experimentally measured coefficient of restitution, e_{dry} , is employed to assign the normal damping constant. The simulated bulk remaining volume in the reservoir was compared to that measured in laboratory experiments (Figure 1/right) to select the most feasible friction coefficient f .

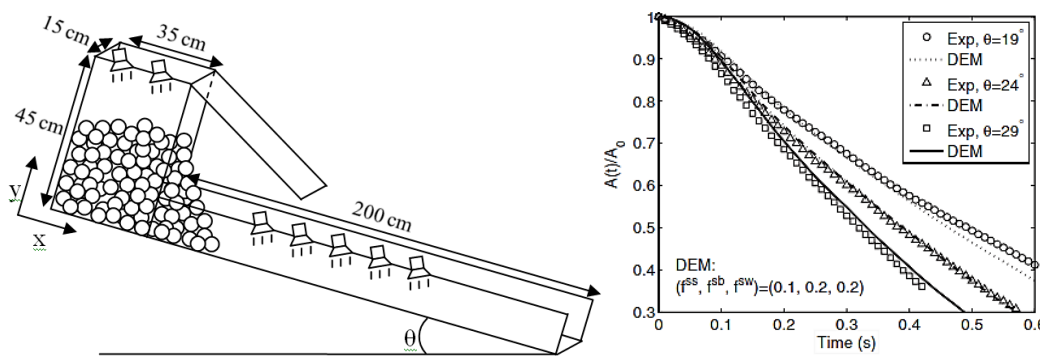


Figure 1. (left) schematic diagram of the lab-scale calibration flume whose dimension and materials were used in the DE simulation; (right) extracting the most feasible friction coefficient pair by comparing the simulated temporal profile of the normalized projection to that measured in the experiments;

The simulated dynamics with the best-fitted f (0.1 for sphere-sphere, 0.2 for sphere-base and sphere-wall contact) compares very well to the measured dynamics on individual grain trajectory (Figure 2) and bulk instantaneous velocity depth profiles at different streamwise locations (Figure 3) down a reservoir inclined at 19° while the instantaneous grain packing configuration and velocity

magnitude at different moments throughout the avalanche are provided in Figure 4. General agreement on the simulated to the measured velocity depth profile was also found for velocity profile at much greater inclination at 24° and 29° (Figure 5 left/right)

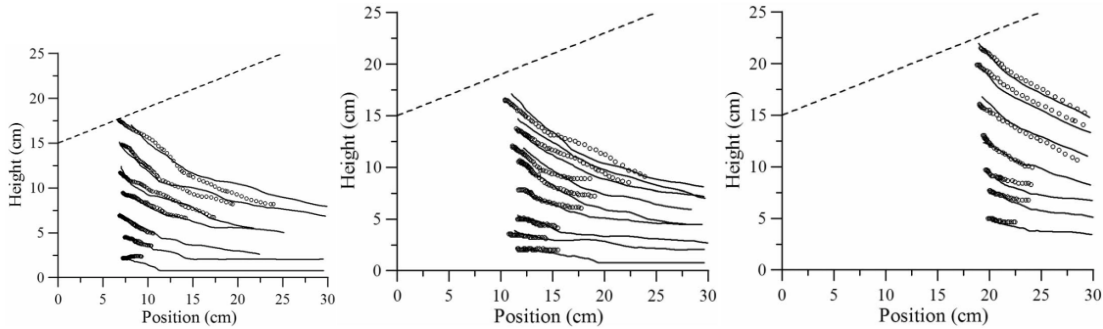


Figure 2 Comparison of the simulated and the measured trajectories of individual spheres moving next to the reservoir wall in a dry granular avalanche at 19° inclination at the (a) rear ($x=8\text{cm}$), (b) central ($x=16\text{cm}$), (c) front ($x=24\text{cm}$) locations: experiment, \circ ; simulation, —. The dashed line indicates the original packing surface.

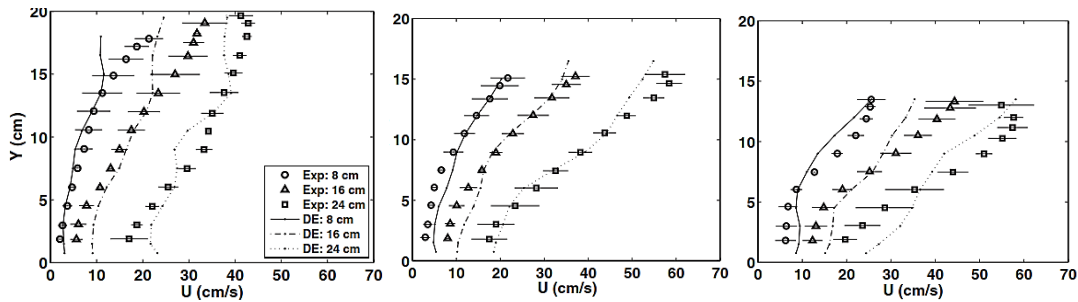
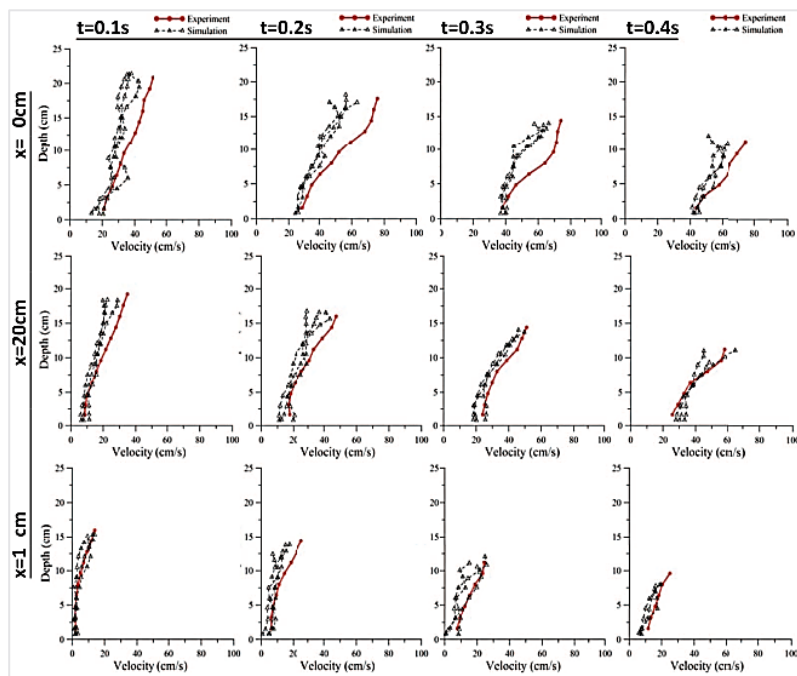


Figure 3 Comparison of the simulated (in symbols) and the measured instantaneous bulk velocity profile at different times after opening the gate: (a) 0.1 s, (b) 0.2 s, (c) 0.3 s. The velocity was examined at three streamwise locations from the reservoir upstream corner at $x = 8, 16,$ and 24 cm .



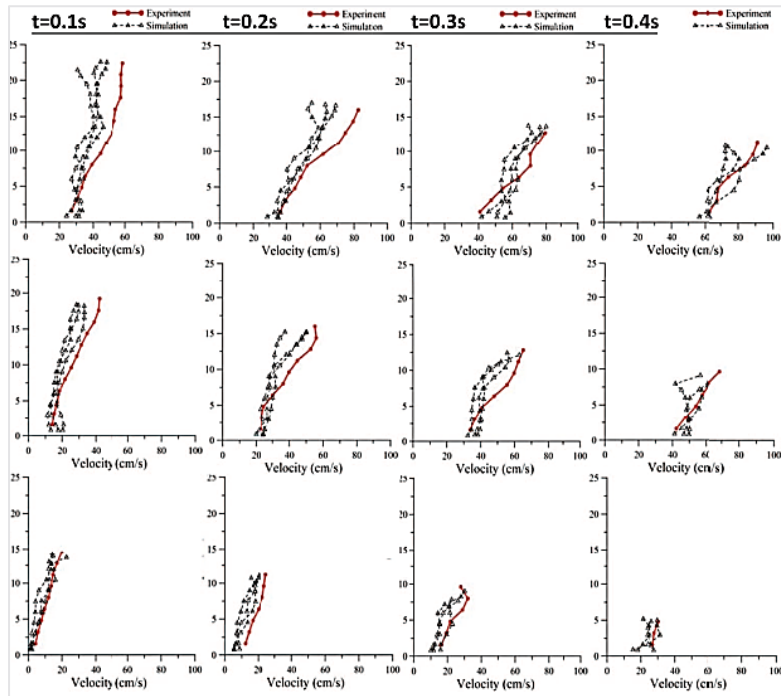


Figure 3 Comparison of the instantaneous bulk velocities from three experiments and simulations at different times and positions for the avalanche down the flume inclined at (top) 24° and (bottom) 29° from the horizontal.

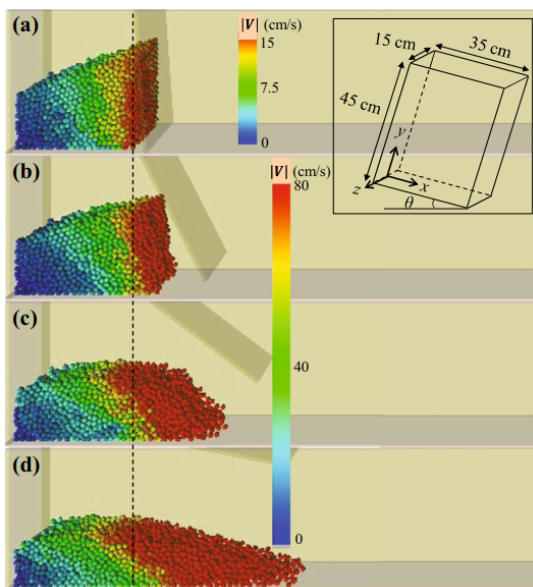


Figure 4 Instantaneous sphere velocity magnitude (in color) and bulk configuration at $t=0.01, 0.1, \text{ and } 0.2\text{s}$. The reservoir and the Cartesian coordinate system set to the center of the reservoir rear lower edge with x parallel to the base, y normal to the base, and z perpendicular to sidewalls

Discover non-constant wall friction coefficient μ_w and attribute it to grain rotation

From DE simulation, lateral wall friction coefficient $\mu_w(x,y)$ was evaluated by the instantaneous stress components by summing all the particle-wall interaction forces in an averaging square over a short smooth time of 0.01s. Instantaneous contour maps of $\mu_w(x,y)$ at $t = 0.01, 0.1, 0.2,$ and 0.3 s are shown in **Figure 5** showing non-uniform and transient nature, contrasting the common assumption as a constant in most granular flow models. When local instantaneous μ_w was also examined with respect to local I (local normal stress) in **Figure 6/left**, sharp and nonlinear rise of μ_w with I was observed over $0 < I < 0.05$ which saturates quickly to the plateau of sphere-wall pure sliding friction coefficient $I^{sw}=0.2$ above $I > 0.09$ (calibrated as marked in the caption of **Figure 1**). The fact that μ_w saturates much faster than μ may explain why constant μ_w seems to be a feasible assumption in most continuum models for steady flows. Nonetheless, the apparent scattering suggests dependence on a different flow variable and we looked into grain rotation as suggested by experimental visualization image in **Figure 6/right**. It is clear that the marker sphere started with pure sliding at the onset of bulk avalanche and developed concurrent spin and rotation when moving towards the base during the course of an avalanche.

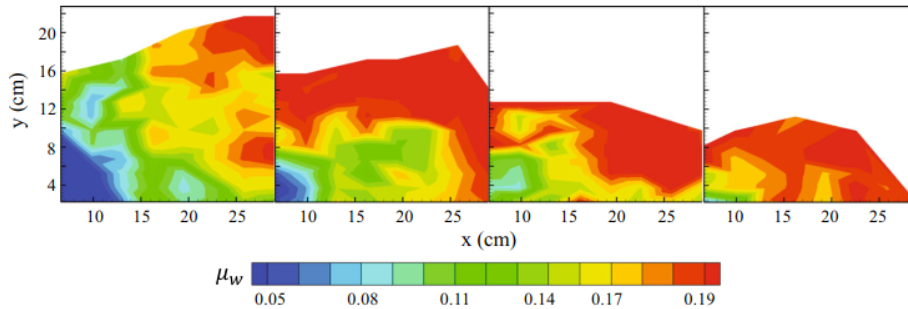


Figure 5 Instantaneous contour maps of $\mu_w(t, x, y)$ at $t=0.01, 0.1, 0.2,$ and 0.3 s.

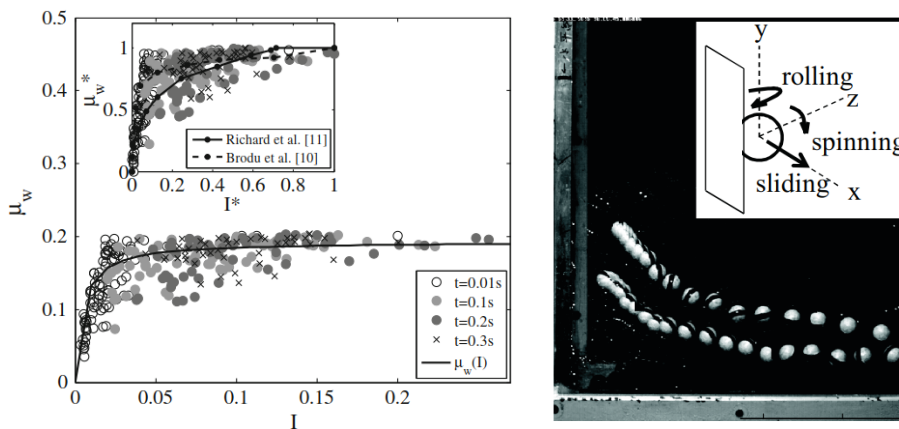


Figure 6 (left) Instantaneous μ_w - I data and the line is a least-square fitted relation $\mu_w=0.002+0.19/(1+0.005/I)$. The inset compares the normalized $\mu_w^*-I^*$ data from this work and the cited references; (right) Visualization of how individual sphere changed its orientation along with the avalanche process. Possible modes for individual sphere motion—sliding, rolling, and spinning—are sketched in the inset.

The simulation data was then analyzed for regional arithmetic mean of the three angular velocity components $\omega_x, \omega_y,$ and ω_z to estimate its effect on sliding contact via the ratios, $\omega_x^*=\omega_x/|\partial v/\partial z|,$ $\omega_y^*=\omega_y/|\partial u/\partial z|$ and $\omega_z^*=\omega_z/[(\partial v/\partial z)^2+(\partial u/\partial z)^2]^{1/2}$. The three angular speed ratios are added up to

estimate a total effect and presented as instantaneous contours in **Figure 7**. It is noted that the spatial distribution of low-to-high ω_i^* or $\sum \omega_i^*$ corresponds very well to the high-to-low $\mu_w(x,y)$ and their correlation can be fitted into Gaussian-like distribution as shown in **Figure 8**. It is this close correspondence that urges us to seek a theoretical modeling considering how grain rotation modifies sliding contact.

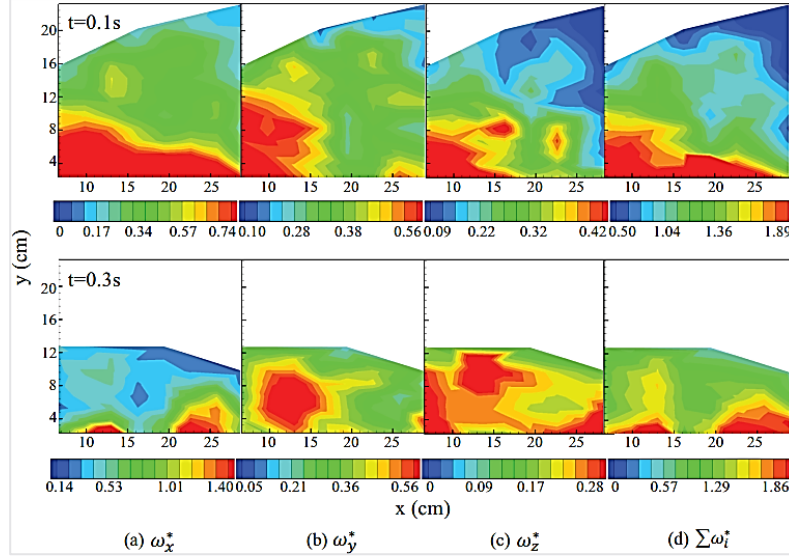


Figure 7 Instantaneous contour of normalized angular speed ω_x^* , ω_y^* , ω_z^* and their lumped sum adjacent to the wall at $t=$ (top) 0.1s and (bottom) 0.3s after the bulk was released.

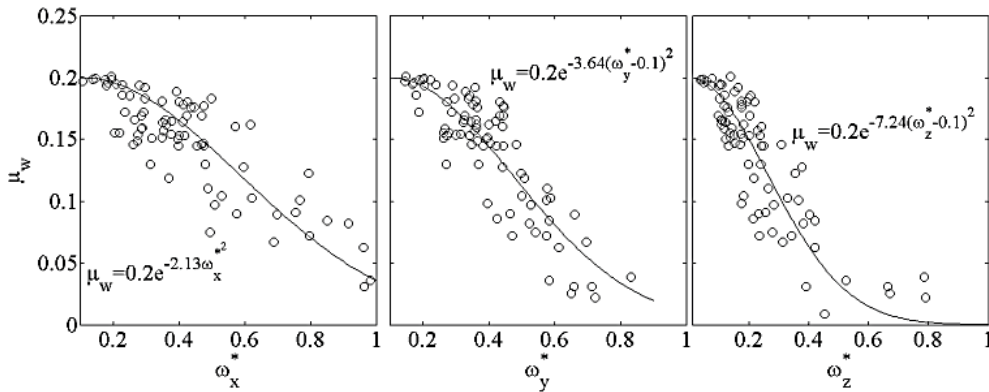


Figure 8 Decay of instantaneous μ_w ($t=0.1s$) as a function of local angular speed ratios and the best fit

Consider a sphere that possesses sliding and angular velocity of u and ω at its center of mass as sketched in **Figure 9**. The total velocity at the contact point on the reservoir wall, $u_{tot}=u+\omega \times r$, can divert total relative velocity, into different direction over *the contact area* on the reservoir walls to render lower sliding friction. In a flow-fitted coordinate system, this becomes

$$\tilde{u}_{tot} = (u'_x + R\omega'_y - r \sin \theta \omega'_z)e_{\perp} + (-R\omega'_x + r \cos \theta \omega'_z)e_{\parallel} + (u'_z + r \sin \theta \omega'_x - r \cos \theta \omega'_y)e_z,$$

We assume that pure sliding took place within an infinitesimal contact surface dA on the contact area to render a hindrance, $f p dA$, against local u_{tot} where f and P are the sliding friction coefficient and the normal stress, respectively. Direct integration over a circular contact area A_c gives the total force

$$\vec{F} = -fP \int \vec{u}_{tot} / |\vec{u}_{tot}| dA$$

As sphere free motion away from the wall is nearly impossible in a dense packing, only the velocity components against the wall were considered as

$$\tilde{u}_{2D} = \tilde{u}_= \{ [1 + \Omega(\tilde{\omega}_{||}^* - r^* \sin \theta \tilde{\omega}_z^*)] e_= + \Omega(-\tilde{\omega}_\perp^* + r^* \cos \theta \tilde{\omega}_z^*) e_{||} \}$$

with $\omega_x^* = \omega'_x / |\omega'|$, $\omega_y^* = \omega'_y / |\omega'|$, $\omega_z^* = \omega'_z / |\omega'|$, and $r^* = r/R$. The dimensionless $\Omega = R|\omega|/u_=$ is the primary parameter for the influence degree of sphere rotation on total sliding friction and will be referred to as the *rotation index*. Secondary effect comes from the relative magnitude of each angular velocity components.

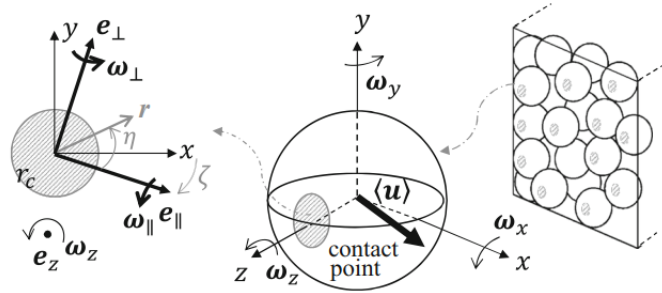


Figure 9 Illustration of model concepts (Right/middle subplot): sphere in contact with reservoir wall possess sliding and angular velocity components at its center of mass; (left subplot): model parameters and dynamics variables in $e_{||}/e_{\perp} - e_z$ coordinate system.

The friction component against $u_=$ can then be computed so that an effective wall friction coefficient can be expressed as

$$\mu_w = |F|=/P = fK(\Omega, \tilde{\omega}_i^*)$$

with a pure-sliding friction coefficient and a decay function

$$K(\Omega, \tilde{\omega}_i^*) = \int_0^{2\pi} \int_0^{r_c/R} \frac{[1 + \Omega(\tilde{\omega}_{||}^* - r^* \sin \theta \tilde{\omega}_z^*)]}{\{ [1 + \Omega(\tilde{\omega}_{||}^* - r^* \sin \theta \tilde{\omega}_z^*)]^2 + [\Omega(-\tilde{\omega}_\perp^* + r^* \cos \theta \tilde{\omega}_z^*)]^2 \}^{1/2}} r^* d\theta dr^*$$

It is clear that zero rotation with vanished rotation index $\Omega=0$ returns $K=1$ to recover Coulomb friction from pure sliding. A nonzero Ω leads to $K < 1$ as sphere rotation diverts friction on the contact area into different directions to give a lower effective value μ_w . For practical applications, we reexamined the expression and suggest to omitting the terms involved with r^* as it is bounded by the contact area radius, r_c^* , that is always several orders of magnitude smaller than unity if estimated as an elastic Hertzian contact. Such an approximation permits an explicit decay function, denoted

$$K_0(\Omega, \tilde{\omega}_i^*) = \frac{1 + \Omega \tilde{\omega}_{||}^*}{\{ (1 + \Omega \tilde{\omega}_{||}^*)^2 + (\Omega \tilde{\omega}_\perp^*)^2 \}^{1/2}}$$

Simulated sphere angular speeds were analyzed to find characteristic values for angular components to use in the formula: $(\tilde{\omega}_{||}^*, \tilde{\omega}_{\perp}^*) = (0.3, -0.95)$, $(0.638, -0.62)$, and an assumed case of $(1/\sqrt{2}, -1/\sqrt{2})$. The results obtained via numerical integration seem to bound the value from DE simulation in [Figure 10/left](#) and also fall very closely to the explicit approximation $K_0(\Omega, \tilde{\omega}_i^*)$ in [Figure 10/right](#), supporting its usage.

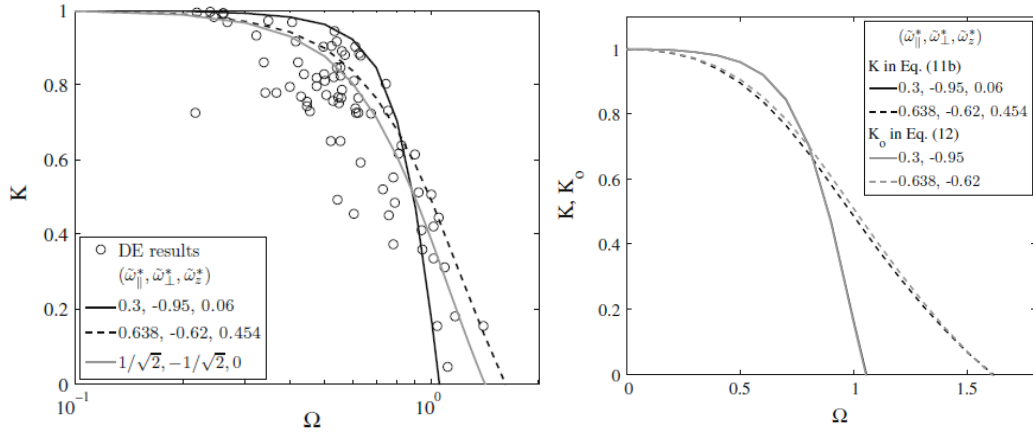


[Figure 10](#) (left) Comparison of the predicted K – Ω with the specific sets of angular speeds to those extracted from DE data; (right) comparison of the full and the reduced model for the decay function

Empirical evidence for grain rotation speeds via a novel image processing method

We went on to seek experimental evidence for how grain angular speeds and the rotation index Ω distribute in space and evolve in time. In the same avalanche experiments, roughly 10-15 marker spheres were inserted manually next to the reservoir wall and across the packing as shown in [Figure 11/left](#). These marker spheres were prepared by randomly gluing 8 circular stickers (diameter 6mm) so that at least one can be captured in each high-speed image (500 frames per second). We applied circular Hough transformation to locate both the spheres and the markers as shown in [Figure 11/middle](#). Next, we assume that the camera frame rate was sufficiently high so that the rotation axis of a marker sphere remained roughly the same through a short image sequence. Hence, the markers located in consecutive images would form an arc in the *moving* reference frame fixed to the sphere center, as illustrated in [Figure 11/right](#). The rotation axis can then be evaluated by the normal vector $n=(A,B,-1)$ of a plane, $E: z'=Ax'+By'+C$, fitted to five consecutive marker locations via a typical quadrature that minimizes the sum of square of residuals as

$$\begin{pmatrix} A \\ B \\ C \end{pmatrix} = \begin{pmatrix} \sum x_i'^2 & \sum x_i'y_i' & \sum x_i' \\ \sum x_i'y_i' & \sum y_i'^2 & \sum y_i' \\ \sum x_i' & \sum y_i' & \sum 1 \end{pmatrix}^{-1} \begin{pmatrix} \sum x_i'z_i' \\ \sum y_i'z_i' \\ \sum z_i' \end{pmatrix}$$

As the camera frame rate was high enough, We also employed The instantaneous segments between consecutive S_i s to approximate an instantaneous tangential velocity as $V_i = [(x'_{i+1} - x'_i)^2 + (y'_{i+1} - y'_i)^2 + (z'_{i+1} - z'_i)^2]^{1/2} / \Delta t$ where $\Delta t = 1/\text{FPS}$ is the elapsed time between two consecutive images (two dots on [Figure 11/right](#)). We averaged out these instantaneous speeds to estimate a mean value V across the short observation time to smooth out fluctuating uncertainty due to sticker location error. From this, we determined the angular velocity magnitude by $\omega = V/R$ and the corresponding angular speed components, ω_x , ω_y , and ω_z with the estimated rotation axis.

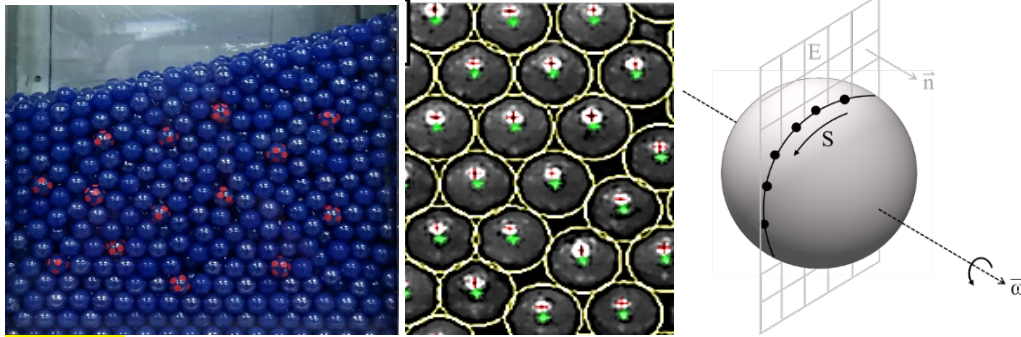
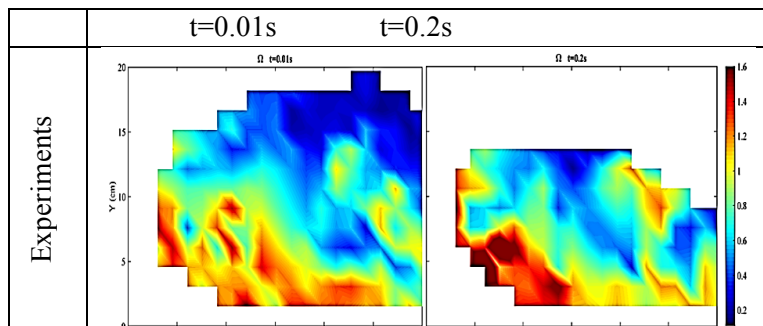


Figure 11 (left) marker spheres with 6 circular stickers distributed randomly across the packing; (middle) located bright spots used to evaluate sphere centers as marked by green +; (right) Illustration for how the rotational axis $\vec{\omega}$ is related to the surface normal vector \vec{n} of a fitted plane E .

As Ω is the primary controlling parameter in the approximate degradation function K_0 , we applied the measured translational and angular sphere speeds to evaluate instantaneous contour of Ω at $t=0.01$ and $0.2s$ in [Figure 12/left](#). The corresponding results obtained from DEM are provided in [Figure 12/right](#) for comparison, showing dynamic similarity to further confirm the physical relevance of the DEM data. These instantaneous $\Omega(t, x, y)$ is examined in view of the contour of $\mu_w(t, x, y)$ at $t=0.01$ and $0.2s$ (shown in [Figure 5](#)) to confirm that the low-to-high distribution of $\mu_w(t, x, y)$ does correlate well to the high-to-low segments of Ω , validating our model speculation.

Lastly, we follow the previous procedure to analyzed the measured angular speeds to estimate two sets $(\omega_{||}^*, \omega_{\perp}^*, \omega_z^*) = (-0.662, 0.524, 0.465)$ and $(-0.747, 0.547, 0.337)$ so that the first two components can be employed in $K_0(\Omega, \omega_{||}^*, \omega_{\perp}^*)$. The so-predicted degradation functions compare reasonably well to the individual data using measured grain angular speeds and those reported from DE simulation and predictions with the simulation-based $(\omega_{||}^*, \omega_{\perp}^*)$ in [Figure 13](#). What remains to be confirmed is to extract μ_w from experiments and the task has been undertaken. Furthermore, it undoubtedly requires further research to formulate grain rotation in terms of bulk property—such as bulk velocity, shear strain rate, or vorticity—to complete a mathematical model at flow size level.



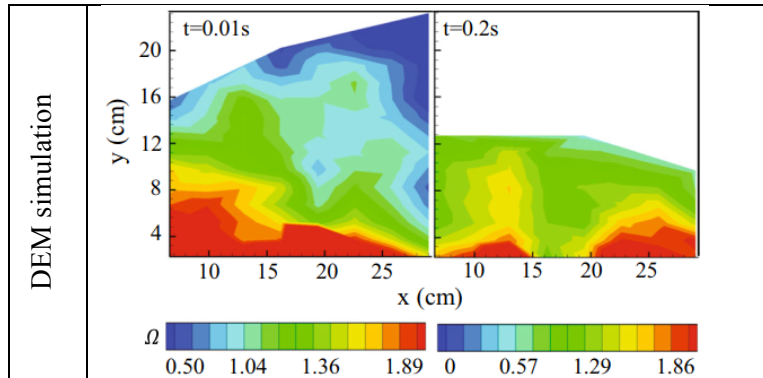


Figure 12 Instantaneous contours for rotation index Ω from experiments (top row) and DEM simulation (bottom row) at $t=0.01s$ and $0.2s$ (left and right subplots).

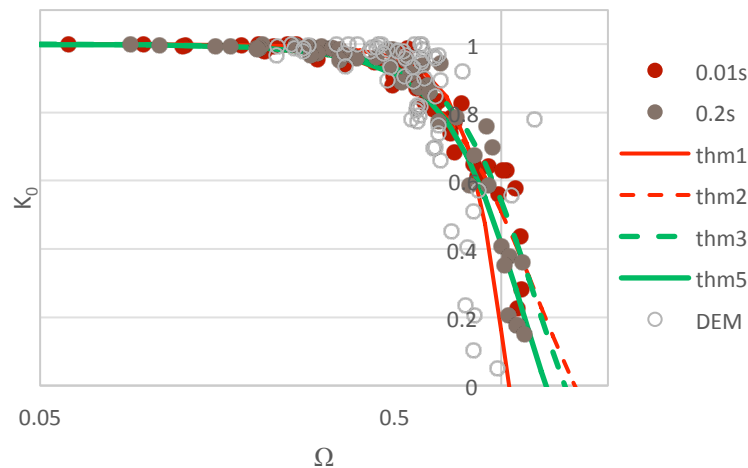


Figure 13 Comparison of K_0 - Ω using sphere angular information from experiments at $t=0.01$ and $0.2s$ after the onset of bulk avalanche and from DE simulation. The four predictions adopt characteristic angular components estimated from both measured and simulated data: $(\hat{\omega}_1^*, \hat{\omega}_2^*) = \text{Thm1} (0.3, -0.95)$, $\text{Thm2} (0.638, -0.62)$ from DE simulation; $\text{Thm3} (-0.662, 0.524)$ and $\text{Thm5} (-0.747, 0.547)$ from experiments.

Effects of density variation on models of dense compressible granular flows

Flow of granular material have been extensively investigated in recent years and the ultimate goal is to capture the flow dynamics under various flow conditions that can be classified as gas, quasi-static and dense regime. The kinetic theory has been developed to describe flows in collisional gas-like regime and visco-elastic or visco-plastic models have been formulated for bulk dynamics in the quasi-static regime using the analogy to soil plasticity models. In the intermediate dense flow regime, there has been no unified framework to capture the transition from regimes to regimes and an empirical relation has been fitted to link pertinent flow variables. This is known as the $\mu(I)$ rheology relation that describe the shear-to-normal stress ratio as monotonic function of bulk inertial number as $\mu(I) = \mu_s + (\mu_2 - \mu_s)/(I_0/I + 1)$ (Jop et al., 2006). Concurrent modification on bulk density, in terms of solid volume fraction ϕ , density has also been studied in 2D simple shear flows and the so-called dilatation law was proposed by Da Cruz (2005) as $\phi(I) \cong \phi_M - AI$. For steady surface flows down an inclination, kinetic theory has predicted non-uniform density depth profile in the collisional

regime (Johnson 1990, Ancey...). Nonetheless, most works seeking numerical or theoretical solutions assume negligible effect of density variation including even invoking the $\mu(I)$ rheology in the momentum equation (Lagrée et al., 2011; Gray & Edwards, 2015).

An integrated formulation based on μ -I and ϕ -I relations

It is hence desired to develop a numerical framework that incorporates density variation. The governing equations for compressible granular flows that integrate both $\mu(I)$ and $\phi(I)$ relations may be formulated as

$$\text{C-E} \quad \frac{\partial(\rho_P \phi)}{\partial t} + \nabla \cdot (\rho_P \phi \mathbf{V}) = 0 \quad (1)$$

$$\text{x-ME} \quad \frac{\partial(\rho_P \phi u)}{\partial t} + \frac{\partial(\rho_P \phi u^2)}{\partial x} + \frac{\partial(\rho_P \phi uv)}{\partial y} = \nabla \cdot (\sigma_{ij}) \quad (2a)$$

$$\text{y-ME} \quad \frac{\partial(\rho_P \phi v)}{\partial t} + \frac{\partial(\rho_P \phi uv)}{\partial x} + \frac{\partial(\rho_P \phi v^2)}{\partial y} = \nabla \cdot (\sigma_{ij}) \quad (2b)$$

Constitutive relation:

$$\sigma_{ij} = -P\delta_{ij} + \tau_{ij} = -P\delta_{ij} + \frac{\mu(\phi)A^2}{|\dot{\gamma}_{ij}|(\phi_M - \phi)^2} \rho_P d^2 |\dot{\gamma}_{ij}|^2 \dot{\gamma}_{ij} \quad (3)$$

$$\text{Equation of state: } P = \frac{A^2}{(\phi_M - \phi)^2} \rho_P d^2 |\dot{\gamma}_{ij}|^2 \quad (4)$$

Density variation is taken into account in the pseudo-thermal equation of state in (4).

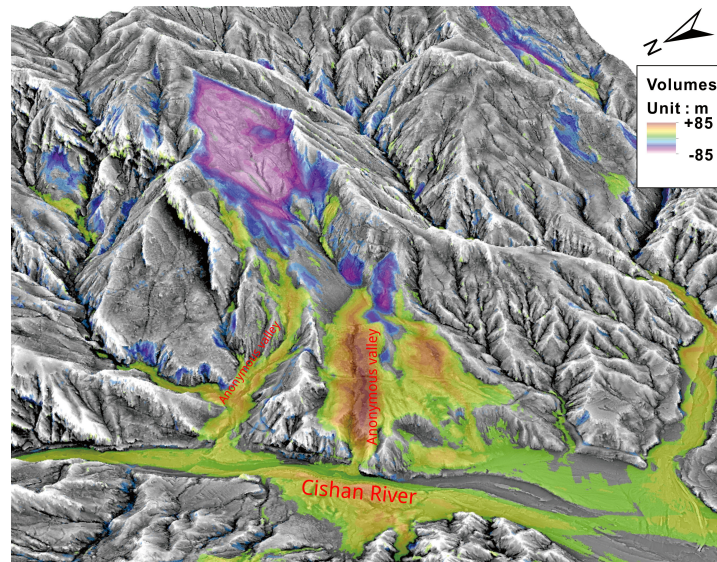
To solve this set of non-linear coupled equation, we plan to try firstly to extend the conventional Riemann solver for compressible gas flows when the system remains hyperbolic. However, when the flow approaches a jamming state when $\phi \rightarrow \phi_M$, unbounded terms appear in the equations to destroy its hyperbolic feature and hence a different numerical scheme is required. For that situation, pressure-implicit-splitted-operator (PISO) numerical scheme developed for conventional Navier-Stokes equations may be worth a try.

Applications in the real world.

Right now, the short-term research goal is to develop a numerical framework that solves the compressible granular flow equations to investigate the effect on non-constant density on bulk dynamics. A long-term perspective is to provide a platform on which different constitutive models and models of boundary conditions can be tested and compared to real flow phenomenon. From systematic comparisons, we should have a better idea for how to select the most feasibly constitutive relation and boundary condition in view of flow types.

Task 6: Code to code validation.

The Hsiaolin landslide, Kaohsiung City, southern Taiwan, was chosen as the example for code validation. The landslide was triggered by the excessive rainfall brought to Taiwan by the Morakot typhoon on the 9th August 2009. The landslide was a deep-seated avalanche of which the volume was about $24 \times 10^6 \text{ m}^3$ with an average depth 42 m. The main scar area is about $570 \times 10^3 \text{ m}^2$. The 3D view is shown in the next figure and the detailed description of the landslide is referred to Kuo et al.



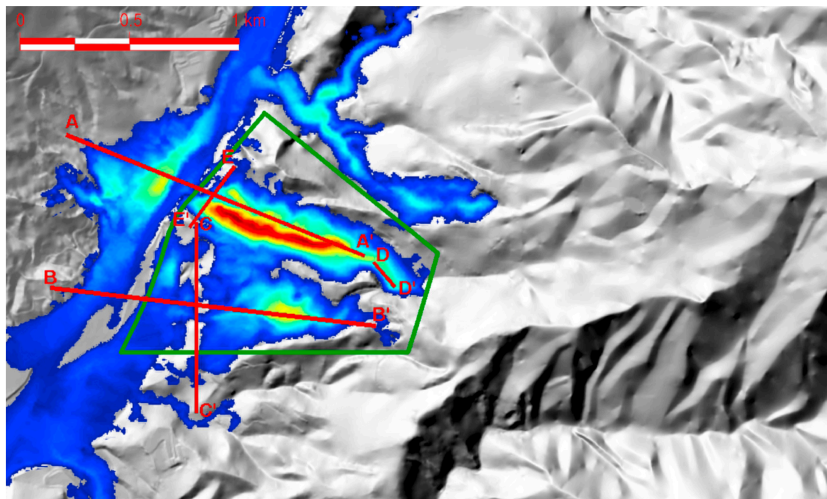
3D view of the Hsiaolin landslide site. The blue-purple area is the scar zone and the red-green-yellow area is the deposit zone.

The landslide was selected for the code comparison. The landslide volume and the topographic surface were obtained from digital terrain models (DTMs) that had been acquired on 7, Jan., a regular-basis survey, and on 13, Aug., an immediate action to the landslide. The resolution of the DTMs was $5 \times 5 \text{ m}$. For convenience the simulation, the landslide site was set to a $3700 \times 2210 \text{ m}$ computational domain and the resolution of the grids was resampled to $10 \times 10 \text{ m}$. In the present finite volume scheme, the triangular unstructured grids were obtained by diagonally bisecting the rectangular mesh cells. The 3D view, where the scar area is the blue-purple colored zone and the deposit is the red-green-yellow zone. The deposit is mainly distributed in three branches of anonymous valleys and in the Cishan River. The landslide mass immediately formed a blockage dam and subsequently broke after another twenty minutes or so. The dam break caused a much wider spread of the deposit mass in the Cishan River. In the code validation task against the real measurement, this second dam break event should be excluded from the validation.

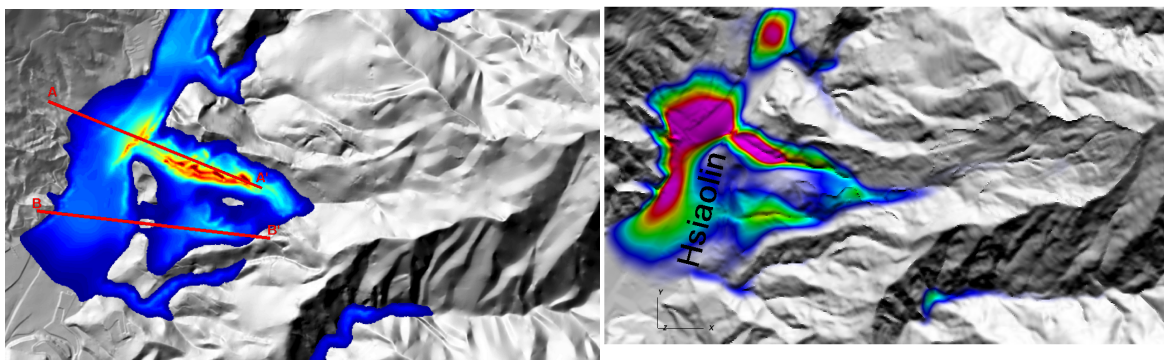
Due to the space limit of the report, we focus on the comparison of the final deposit stage. The solid red lines are profiles to compare detail flow motion which is abbreviated. The green boxed area is the deposit zone that was not affected by the subsequent dam break event. The deposit depth of this area was used in the optimization procedure for the best rheological parameters. Outside (north to) the main deposit area, there is a third thin but wide spread deposit is also found. Because of its much smaller volume compared to the main deposit, it is considered a secondary deposit and is omitted in the current comparison.

Figure shows the deposit comparison between the results of non-oscillatory central difference scheme and the present finite volume scheme. On the left, the simple Coulomb friction law was used. The optimized friction angle is found to be 11.47° , whereas on the right hand side, the friction angle of the present finite volume scheme was set to 14.2° . Noticeably, a larger friction angle was obtained to achieve a similar deposit zone. The main reasons for this discrepancy may arise from: 1) the present Riemann solver based scheme has less numerical diffusivity in comparison to the central finite difference scheme, 2) the unstructured surface grids effectively provides a smoother surface and grossly a finer grid resolution than the previous quadrilateral one. To compensate this additional numerical landslide mass mobility, a larger friction coefficient is reached. Further quantitative comparison will be reported in a designated paper.

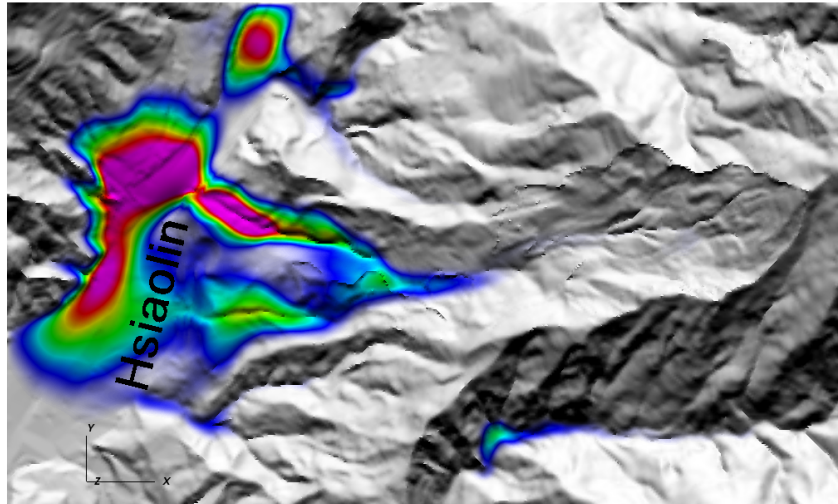
Ref: Kuo, *et al.*, 2011, The landslide stage of the Hsiaolin catastrophe: simulation and validation, *J. Geophys. Res.*, **116**, F04007.



Hsiaolin area, measured of deposit depths after the landslide occurred on 9 August 2009, after Typhoon Morakot struck Taiwan. Measurement was done after the breach of the dam formed on the river. Part of the deposit has been moved downstream by the breach on the Cishan River.



Computed deposit depth using finite volume method on “curved surface” represented by a piecewise triangular mesh.



Computed deposit depth using finite volume method on “curved surface” represented by a piecewise triangular mesh.

2. Record of activities

Taiwan Team Visiting France for workshop

Modeling of dry granular flows, CIRM Marseille: September 8 to September 13 2014.

Sergey Gavriluk, Chih-Yu Kuo, Chyan-Deng Jan, Boniface Nkonga.

July 3 to July 13 2014 : Numerical Methods Advances for Numerics

Close work of *Key-Ming Shyue* and *Boniface Nkonga* on the Numerical Methods: Implicit and Thin interpolation.

14 Nov. - 15 Dec 2014. The post-Doct *Jeaniffer Vides* visits at Taiwan. Development of software for shallow water flows over curved topography.

08 april 2015 : Workshop « Theoretical and experimental study of granular media », National Taiwan University, Dpt. of Mathematics. *S. Gavriluk, Keh-Ming Shyue, Chi-Yu Kuo, Fuling Yang, Yih-Chin Tai.*

07 to 10 July 2015 : *Chi-Yu Kuo and Yih-Chin Tai* visit at INRIA Sophia-Antipolis

July 8th 2015 : Annual meeting at Inria Sophia Antipolis :

<https://team.inria.fr/amoss/fr/events/>

- *A new model of long dispersive waves on shear flows*, *S. Gavriluk*
- *Experimental observation on surface undulations over erodible bed*,

Yih-Chin Tai, Chin-Kai Cheng and Chih-Yu Kuo

- **Modified shallow water equations for significant bathymetry variations**, *D. Clamond*
- **Well balanced ALE : simple time dependent mesh adaptation for balance laws**, *M. Ruchiotto*
- **A flexible approach for the numerical solution of the Green-Nagdhi equations**, *A.G. Filippini, M. Kazolea, M. Ricchiuto*
 - **Gas kinetic scheme for anisotropic Savage-Hutter Model**, *C.Y. Kuo*
- **Stabilized spectral element approximation of the Saint Venant system using the entropy viscosity technique**, *R. Pasquetti*
 - **On solitary waves for boussinesq's type models**, *M. Colin*
 - **Well-Balanced schemes**, *B. Nkonga*

Aug. 22 to Sep. 01, 2015 : *Fu-Ling Young* visit at IUSTI .

Aug. 22 to Sep. 20, 2015 : *Keh-Ming Shyue*, Invited professor at the University of Marseille.

November 14 to 24, 2015 : *Hervé Guillard*, visit at Taiwan. Study of shear shallow water models. During the stay of HG, a mini-workshop gathering several researchers and students from NTU and Tainan have been organized November 18 and 19.

March 21 to 25, 2015 : *Richard Pasquetti* visit at Taiwan. Viscous stabilization methods, namely the spectral vanishing viscosity (SVV) technique and the entropy viscosity method (EVM), are applied to flows of interest in geophysics.

Aug. 24 to Sep. 15, 2016 : *Cheng-Chuan Lin*, 4th year Phd student of Prof. *FuLing Yang*, have a personal initiation by *B. Nkonga*, on Numerical solvers for compressible granular flow using Mu-I-phi constitutive relation.

Aug. 29 to Sep. 08, 2016 : Modeling of dry granular flows, IUSTI Marseille:

Sergey Gavriluk, Cheng-Chuan Lin, Yih-Chin Tai, Chyan-Deng Jan, Boniface Nkonga.

Oct. 28 to Nov. 11 2016 : **AMoSS closing meeting at Taipei and Tainan.** Mini-symposium at the 12th International Conference on Hydroscience & Engineering iche2016.hyd.ncku.edu.tw/

S. Gavriluk, Keh-Ming Shyue, Chi-Yu Kuo, Fuling Yang, Yih-Chin Tai, B. Nkonga, K.A. Ivanova

3. Production

[1] **K.A. Ivanova, S.L. Gavriluk, B. Nkonga, G.L. Richard**, *Formation and coarsening of roll-waves in shear shallow water flows down an inclined rectangular channel*, Submitted.

[2] **J. Vides, B. Nkonga, Y.C. Tai, C.Y. Kuo**, *Multi-scales approximation of thin flows for curved topography*, 12th Int. Conf. on Hydroscience, & Engineering 2016, to be submitted.

[3] **R. Pasquetti**, *Viscous stabilizations for high order approximations of Saint-Venant and Boussinesq flows*, ICOSAHOM 2016, Rio, June 27-July 1, 2016. Proceeding submitted.

4. Non- Public Information

Detail any information that you do not want to publish on your web site (partnerships, etc.)